

# Drainage through subglacial water sheets

Timothy T. Creyts

Department of Earth and Planetary Science, University of California, Berkeley, California, USA

Christian G. Schoof

Department of Earth and Ocean Sciences, University of British Columbia, Vancouver, British Columbia, Canada

**Abstract.** Subglacial drainage plays an important role in controlling the coupling between glacial ice and the underlying bed. Here, we study the flow of water in thin, macroporous sheets between ice and bed. Previous work shows that small perturbations in water depth for a nearly parallel-sided water film between ice and bed grow unstably because areas with greater water depth have enhanced viscous dissipation that leads to enhanced melting of the ice roof. We argue that in the presence of bed protrusions bridging a water sheet, the sheet can be stabilized by downward motion of the ice roof around protrusions. This should be the case provided the rate of roof closure increases faster with water depth than the rate of viscous dissipation within the sheet. We therefore modify existing theory to include protrusions that partially support the mass of the overlying glacier. Differences in the pressure driving on these protrusions relative to the water sheet drive roof closure. The roof closure rate includes both the effects of regelation and creep normal to the bed as mechanisms by which the overlying ice can move downward, closing the ice–bed gap occupied by the water. The roof closure rate includes the mechanisms of both regelation and creep normal to the bed allowing ice to move downward, closing the ice–bed gap occupied by the water. In order to account for multiple protrusion sizes at the bed (for instance, resulting from an assortment of various-sized sediment grains), we incorporate a method for partitioning overburden pressure among the different protrusion size classes and the water sheet. This method allows prediction of the rates of downward motion for the ice roof. Rates are dependent on the degree of ice–protrusion contact and therefore on water depth. We then investigate the possibility of stable, steady sheet configurations for reasonable parameter choices, and find that these steady states can occur for modest sheet thicknesses at very low effective pressures, as is appropriate for instance of ice streams. Moreover, we find that multiple steady sheet thicknesses exist allowing for the possibility of hydraulic switches between low and high conductivity regimes for the subglacial hydrological system.

## 1. Introduction

Subglacial drainage is one of the main controls on glacier sliding and erosion. Friction at the glacier bed is determined in large part by effective pressure, usually defined as the difference between ice overburden and subglacial water pressure. This is the case for both deformable and rigid glacier beds [*e.g.*, Paterson, 1994, Chaps. 7,8]. For glaciers and ice sheets with water at the bed, any predictive theory of ice dynamics requires a component that describes evolution of effective pressure, that is, a theory for drainage at the ice–bed interface.

To determine the distribution of effective pressure at the glacier bed requires an understanding of the morphology of the subglacial drainage system and of the relationship between water discharge, effective pressure, and hydraulic gradient in individual drainage elements. A drainage system can consist of different types of individual elements: for instance, channels, linked cavities, canals, englacial or groundwater flow, or a combination of any of these [*e.g.*, Fountain and Walder, 1998; Hubbard and Nienow, 1997]. While theories exist for the behavior of individual drainage elements, interactions between any of these elements are not

well understood. As a result, there is no successful spatially extended theory for subglacial drainage at present.

The relationship between water storage and effective pressure in different drainage elements governs interactions between such drainage elements. Here, we consider storage, or local water volume, to be water that connects spatially and transmits hydraulic pressure variations [Fountain and Walder, 1998; Murray and Clarke, 1995; Stone and Clarke, 1993], but we do not consider unconnected storage. Unconnected storage is important for transient processes [*e.g.*, Kamb, 1987] but likely plays a smaller role in steady drainage. If connected water storage increases with effective pressure, then a larger drainage element will tend to draw water away from smaller elements because the larger element is at a lower water pressure. The result is that the drainage system concentrates water in a few large drainage elements fed by smaller ones. Conversely, a setting in which a decrease in water storage corresponds to an increase effective pressure leads to the formation of a distributed water system, in which water is not concentrated in a few central drainage elements.

The classical example of a drainage system that concentrates flow in a few main arteries is a R othlisberger (R-) channel system [R othlisberger, 1972]. In the steady case, large R-channels operate at high effective pressure (or low water pressure) because higher melt rates are facilitated by a wider cross-section, and must be balanced by faster creep closure. This gives R-channel systems an arterial character. By contrast, water storage in subglacial cavities increases at low effective pressure, which allows bigger cavities

to grow. Consequently, linked cavity systems tend to form a distributed drainage network.

Once a drainage system is established subglacially, its response to water input is determined by the relationship between flux on one hand and effective pressure and hydraulic gradient on the other. Usually, systems such as R-channels that contain more water at high rather than low effective pressure will also transmit higher fluxes at high rather than low effective pressure. Conversely, distributed drainage systems such as linked cavities, in which water storage is facilitated by low effective pressures, need not have such a simple, monotonic relationship between effective pressure and flux. For instance, the linked cavity theory of *Fowler* [1987] predicts increasing flux with increasing effective pressure (as R-channel theory does) while the canal theory of *Walder and Fowler* [1994] predicts the opposite. To model a drainage system thus requires the physics that determines water flux at a given effective pressure to be understood.

In short, a theory for subglacial drainage must incorporate two fundamental pieces: a functional relationship between water storage and effective pressure, and a means of determining water flux in terms of effective pressure and hydraulic gradient.

In this paper, we consider these relationships for drainage through contiguous, macroporous water sheets at the ice-bed interface. We envisage water flowing in a gap between ice and bed, with clasts bridging the gap in places and providing partial support for the overlying ice. The mode of drainage we have in mind combines characteristics of both R-channels and linked cavities. As is the case in an R-channel, the gap is assumed to remain open because subsidence (or closure) of the ice roof is balanced by melt that results from heat generation by viscous dissipation in flowing water; but as in a linked cavity system, water volume in the sheet increases with decreasing effective pressure, leading to a distributed configuration.

Sheet-like drainage elements have been considered previously, for instance by *Weertman* [1972] and *Walder* [1982]. The main difference between their notion of a water film and our notion of a water sheet is that we consider an ice roof that is partially supported by contact with the bed — as is also the case in a linked cavity system — while in *Weertman's* and *Walder's* cases, ice and bed are everywhere separated by water, so the ice is effectively afloat on a thin water film. In general, we expect complete flotation of the ice on a thin water film not to occur, but unevenness in the bed to lead to partial contact. As we shall outline next, this is a crucial difference which allows our water sheet to remain stable while *Walder's* film configuration necessarily leads to channelization. From this point forward, when discussing subglacial drainage, we make the distinction that a water sheet has partial contact between the ice roof and sediment floor. On the contrary, a water film everywhere supports the overlying ice as described by *Walder* [1982] and *Weertman* [1972].

Hydraulic sheets will be favored where gradients driving water flow are low and sliding velocities are high, as we argue further in section 2. These locations are generally coincident with low ice overburden gradients. As such, low-gradient ice sheets and glaciers will favor subglacial sheets [e.g., *Kamb*, 2001]. Areas with steep ice thickness gradients, such as those near glacier termini, will not favor sheet development or stability.

It is important to differentiate the sheets we consider from subglacial floods in which overpressured sheets form and subsequently channelize in the manner envisaged by *Walder* [1982]. Field evidence exists for these sheet-like flows [*Björnsson*, 2002; *Jóhannesson*, 2002; *Magnússon et al.*, 2007]. The sheets we consider here are distinct from these short-lived flood-type sheets. We expect the former to exist stably in low discharge/low hydraulic gradient settings. The latter exist in high discharge/low hydraulic gradient settings.

## 2. Motivation

In order to understand how water can flow stably in a subglacial sheet-like configuration, it is necessary to understand what might prevent such sheets from forming. *Walder's* [1982] analysis showing that sheet flows are unstable can be paraphrased as follows. If the sheet thickens locally, water flow through this wider aperture will be faster and more heat will be dissipated. This in turn leads to further local thickening of the sheet and hence to channelization. If we consider a vertically-integrated, two-dimensional case, where heat transport in the along-flow direction is mainly by advection, and diffusion—either laminar or turbulent—governs heat transfer perpendicular to flow, then this positive feedback is suppressed at short length scales by lateral diffusion of heat in the water sheet. For turbulent flow, momentum diffusion associated with eddies can be written using an isotropic eddy diffusivity [*Schlichting*, 1979] and leads to a turbulent heat diffusivity.

Here we argue that if this diffusion is strong enough and there are bed protrusions bridging the water-filled gap between ice and bed, then a sheet configuration can, in fact, remain stable. To illustrate this, we consider the following simple model of unidirectional water flow parallel to the  $y$ -axis. By unidirectional flow we mean that water velocity does not have a component perpendicular to the  $y$ -axis; and consequently, we assume a hydraulic potential  $\phi$  that depends only on  $y$ . Let  $x$  measure distance perpendicular to the  $y$ -axis, and  $H(x, t)$  be water depth, while  $u(x, t)$  is water velocity in the  $y$ -direction. Then the Darcy-Weisbach relationship gives, for steady state velocity,

$$u = -\sqrt{\frac{4H}{\rho_w f_d}} \left| \frac{\partial \phi}{\partial y} \right|^{-1/2} \frac{\partial \phi}{\partial y}, \quad (1)$$

where  $f_d$  is a friction factor and  $\rho_w$  is the mass density of water. We assume here that the water in the sheet is fully turbulent. Other relationships exist for laminar flow [e.g., *Weertman*, 1972]; however, we do not treat them directly. We also model melting of the ice roof as the result of heat transfer from the core of the flow across a thermal boundary layer near the ice surface, in which heat transfer is determined either by near-wall turbulence due to surface roughness or by the thermal conductivity of water if the flow in the boundary layer is laminar. Let  $m$  be melt rate. Then

$$mL = c(T - T_m) - q_0, \quad (2)$$

where  $L$  is latent heat of fusion,  $c$  a heat transfer coefficient for the boundary layer, and  $q_0$  is a background heat flux that can include the geothermal heat flux, heat of sliding, heat diffused through the ice, or other heat sources/sinks.  $T$  is temperature in the interior of the sheet and usually exceeds the melting temperature of ice  $T_m$ . The melt rate  $m$  determines the evolution of the ice-water interface as

$$\frac{\partial H}{\partial t} = \frac{m}{\rho_w}, \quad (3)$$

where we assume that flux divergence is negligible. Temperature  $T$  above is determined by heat dissipation, turbulent diffusion in the sheet, and heat loss to the ice interface,

$$-\frac{\partial}{\partial x} \left( \kappa H \frac{\partial T}{\partial x} \right) = -Hu \frac{\partial \phi}{\partial y} - c(T - T_m), \quad (4)$$

where  $\kappa$  is a turbulent diffusivity in the fully turbulent part of the flow [e.g., *Ng*, 1998]. In writing the temperature

equation (4) as a steady state equation, we have assumed that latent heat terms dominate over specific heat terms. In other words, we have assumed that  $c_p(T - T_m) \ll L$ . With  $L = 3.336 \times 10^5 \text{ J kg}^{-1}$ ,  $c_p = 4218 \text{ J kg}^{-1} \text{ K}^{-1}$  and temperature deviations from the melting point less than a few degrees, this is certainly the case.

To study the onset of channelization, we look at the evolution of small perturbations to a uniform sheet in steady state. The steady state sheet is described by

$$H = \bar{H} := \left(\frac{q_0}{2}\right)^{2/3} \frac{(f_d \rho_w)^{1/3}}{|\partial\phi/\partial y|}, \quad (5a)$$

$$T = \bar{T} := \frac{q_0}{c} + T_m, \quad (5b)$$

$$u = \bar{u} := \sqrt{\frac{4\bar{H}}{f_d \rho_w}} \left|\frac{\partial\phi}{\partial y}\right|^{-1/2} \frac{\partial\phi}{\partial y}, \quad (5c)$$

where  $:=$  means “is defined to be” and we look at harmonic perturbations of the form

$$H = \bar{H} + H' \exp(ikx + \omega t), \quad (5d)$$

$$T = \bar{T} + T' \exp(ikx + \omega t), \quad (5e)$$

$$u = \bar{u} + u' \exp(ikx + \omega t). \quad (5f)$$

Here,  $k$  represents wavenumber ( $= 2\pi/\text{wavelength}$ ), while  $\omega$  is a growth rate ( $= 1/e\text{-folding time}$ ) associated with the perturbation. We use barred and primed variables to denote average and perturbed variables, respectively. The perturbation grows exponentially if  $\omega > 0$  and shrinks if  $\omega < 0$ .

Substituting these in the governing equations and performing a standard linearization yields the following:

$$u' = -H' \sqrt{\frac{1}{f_d \rho_w \bar{H}}} \left|\frac{\partial\phi}{\partial y}\right|^{-1/2} \frac{\partial\phi}{\partial y}, \quad (6a)$$

$$k^2 \kappa \bar{H} T' = -(\bar{H} u' + H' \bar{u}) \frac{\partial\phi}{\partial y} - c T', \quad (6b)$$

$$\omega H' = \frac{c T'}{\rho_w L}. \quad (6c)$$

Eliminating  $u'$ ,  $H'$ , and  $T'$  from these equations and solving the resulting linear equation for  $\omega$  gives the following equation for growth rate,

$$\omega = \frac{3\bar{u}(\partial\phi/\partial y)c}{2\rho_w L(c + \kappa \bar{H} k^2)}, \quad (7)$$

where  $\omega$  is always positive, reflecting *Walder's* [1982] positive feedback.

However, this mechanism is suppressed at short wavelengths and  $\omega \rightarrow 0$  as  $k \rightarrow \infty$ . Damping of the positive feedback at short wavelengths is because of turbulent diffusion. The maximum growth rate occurs at infinite wavelength ( $k = 0$ ), where  $\omega = 3\bar{u}/(2\rho_w L)$ . Turbulent diffusion reduces growth rate to half this maximum when  $k = \sqrt{c/(\kappa \bar{H})}$ , corresponding to a wavelength  $2\pi\sqrt{\kappa \bar{H}/c}$ . Hence the wavelength at which unstable growth of the sheet begins to be suppressed noticeably increases with turbulent diffusivity  $\kappa$ .

Consider then what happens if there are bed protrusions spaced at distances at which *Walder's* positive feedback is strongly suppressed. In this case, there is the possibility of distributed sheet-like drainage. The sheet that exists between these protrusions is still unstable, but local thickening will be slow. Suppose the timescale for this thickening is less than the timescale on which ice moves over the distance between bed protrusions due to sliding. *Walder's* feedback then causes negligible differences in melting between neighboring parts of the ice roof in the time taken for the ice roof to be advected over bed protrusions. Any differences in melting

between neighboring parts of the roof will therefore be dominated by local changes in sheet thickness associated with protrusions and dips in the bed, rather than by *Walder's* feedback. We assume that the effect of ice being advected over these protrusions and dips is to smooth out any local differences in melting over time, as a part of the ice roof that experiences excess melt when positioned over a dip in the bed will at a later stage experience reduced melt when it has moved over a bed protrusion. Moreover, repeated contacts with bed protrusions will also mechanically deform the ice roof, and serve to even out the ice roof.

Therefore, we expect that unstable thickening is suppressed altogether at this length scale, leaving only the possibility of unstable thickening on longer length scales. Specifically, if  $l$  is the spacing between bed protrusions and  $u_b$  is sliding velocity, then we expect unstable thickening to be suppressed when the time taken for ice to travel between bed protrusions  $l/u_b$  is short compared with the growth timescale  $1/\omega$  computed for wavelengths comparable to  $l$ ,  $k \sim 2\pi l^{-1}$ , or in other words, when

$$\frac{3l|\bar{u}||\partial\phi/\partial y|}{2\rho_w L u_b [1 + \kappa \bar{H} 4\pi^2/(cl^2)]} \ll 1. \quad (8)$$

This suppression is obviously favored by slow water flow rates  $\bar{u}$  (*i.e.*, low hydraulic gradients  $\partial\phi/\partial y$ ), by high sliding velocities  $u_b$ , and by small spacings  $l$  between bed protrusions. The first two of these conditions are clearly consistent with ice stream-type motion, while the latter is a function of local bed geometry. For any of these cases, though, we would expect drainage to be distributed across the ice–bed interface in a sheet.

The argument above deals only with wavelengths up to the obstacle spacing  $l$ , and does leave open the possibility of unstable thickening at longer wavelengths. However, at these longer length scales, different physics applies as interactions between bed protrusions and the ice roof must be taken into account. The remainder of this paper considers these interactions and their implications for the behavior of subglacial water sheets.

### 3. Model for sheet closure

The basic process by which a sheet is stabilized at long wavelengths is through downward motion of the ice roof. Suppose the sheet thickens locally, so there is less contact between ice and bed. If bed protrusions partially support the weight of the overlying ice (*i.e.*, effective pressure is positive), then the reduction in contact will lead to enhanced downward motion of the ice, suppressing further thickening and stabilizing the sheet. To quantify this, we construct a model of the downward ice motion.

We envision downward closure to involve two principal processes: viscous creep of ice between supporting protrusions and pressure melting around individual protrusions. Consider the ice roof between two supporting protrusions. Downward motion of the roof can result from viscous flow between these two support points. If their spacing is  $l_e$  and an effective stress  $\sigma_e$  is available to drive the viscous sagging of ice between them, then the resulting downward velocity can be estimated as,

$$v_c = \mathcal{A} |\sigma_e|^{n-1} \sigma_e l_e, \quad (9)$$

where  $\mathcal{A}$  and  $n$  are the usual parameters in Glen's law [*Paterson*, 1994, Chap. 5]. This equation is based on a simple scaling argument: stresses of size  $\sigma_e$  acting over a length scale  $l_e$  result in velocities of magnitude given by (9). In

reality, if  $v_c$  is mean downward velocity, then there would be an additional factor on the right-hand side whose calculation for a given model geometry is beyond the scope of this work. Implicit here is only that this factor is of  $O(1)$ .

The stress  $\sigma_e$  in equation (9) can be identified for now with the overall effective pressure  $p_e$ , defined as the difference ice overburden  $\sigma_i$  and water pressure  $p_w$ , so  $\sigma_e = p_e$  where  $p_e \equiv \sigma_i - p_w$ . When we generalize our theory later to the case of multiple protrusion sizes,  $\sigma_e$  in (9) becomes the stress that is available to drive viscous sagging between support points, which can be less than  $p_e$ .

In addition, the ice surface can move downward through melting around the supporting protrusions. We assume that this regelation process operates as described by *Nye* [1967]. The regelation velocity that results can be parameterized in a simple form as follows. If the ice is at the pressure melting point throughout, then a pressure difference  $\Delta\sigma$  in the ice near the contact with the bed protrusion will cause a temperature gradient that leads to a melt/freeze pattern that allows the ice to move downward [*Paterson*, 1994, Chap. 7]. This temperature gradient will be of magnitude  $\beta\Delta\sigma/r_e$ , where  $r_e$  is a radius of ice-protrusion contact area and  $\beta$  is the rate of change of ice melting temperature with pressure from the Clausius-Clapeyron relationship [e.g., *Wagner et al.*, 1994]. If  $K$  denotes thermal conductivity, then the associated heat flux is  $K\beta\Delta\sigma/r_e$ , leading to a regelation velocity

$$v_r = \frac{K\beta\Delta\sigma}{\rho_i L r_e}. \quad (10)$$

We compare this formulation of temperate regelation with related work in *Rempel* [2008] in appendix A.

The regelation process described here is driven by the pressure difference  $\Delta\sigma$  around the contact area between ice and the bed protrusion. This is related to effective stress, and we expect  $\Delta\sigma$  to increase with  $\sigma_e$ . More accurately, we can estimate  $\Delta\sigma$  as follows. Consider an arbitrary area  $S_i$  of the lower boundary of the ice that will be partially in contact with the bed and partially supported by the water sheet. Let overburden stress  $\sigma_i$  act normal to this area. Denote by  $S_s$  the part of this area that is in contact with the bed protrusions, and let  $\sigma_s$  be normal stress at these ice-bed contacts. Then  $S_w = S_i - S_s$  is the part of the ice roof in contact with water, and we denote water pressure by  $p_w$ . Force balance requires

$$S_i\sigma_i = S_w p_w + S_s\sigma_s, \quad (11)$$

so that

$$\Delta\sigma = \sigma_s - p_w = \frac{S_i}{S_s}(\sigma_i - p_w) = \frac{S_i}{S_s}\sigma_e. \quad (12)$$

In other words, the driving pressure difference  $\Delta\sigma$  in the regelation process is effective pressure divided by the fraction of the ice roof occupied by ice-bed contacts. Equation (10) therefore becomes

$$v_r = \frac{\beta K}{\rho_i L r_e} \frac{S_i}{S_s} \sigma_e. \quad (13)$$

The total downward motion  $v$  of the ice is then simply given by the superposition of viscous creep and regelation,

$$v = v_c + v_r. \quad (14)$$

The total ice velocity  $v$  is a function of effective pressure  $p_e$ . It is also a function of water depth  $H$ , as an increase in  $H$  is likely to reduce the contact area  $S_s$  (and hence also reduce the contact radius  $r_e$  while increasing the contact spacing  $l_e$ ), leading to an increase in regelation velocity  $v_r$  as well

as creep velocity  $v_c$ . It is precisely this kind of increase in  $v$  with increasing  $H$  that we expect to stabilize the water sheet against thickening due to enhanced viscous dissipation. To compute the relationship between  $v$ ,  $p_e$ , and  $H$  and establish whether a stable sheet flow is possible therefore requires us to specify how  $S_s$ ,  $r_e$ , and  $l_e$  depend on sheet thickness.

A real bed likely has multiple protrusion sizes, and this can have a large effect on the roof closure velocity  $v$ . For instance, increases in  $H$  can lead to smaller protrusions losing contact with the ice altogether and leave only larger sizes to support the ice roof of the sheet. The net result will be faster downward motion of the ice. This increase in velocity also turns out to be a major component in the stabilization of the water sheet, and we generalize equations (9) and (13) to account for multiple obstacle sizes. Subsequently we address how the geometrical parameters corresponding to  $S_s$ ,  $r_e$ , and  $l_e$  for either a single or for multiple obstacle sizes depend on water depth  $H$ , and then we compute numerical examples in section 4.

### 3.1. Sheet closure with multiple protrusion sizes

We consider size classes of bed protrusions with distinct radii  $R_1, R_2, \dots, R_j, \dots, R_N$  as was done by *Lliboutry* [1979]. Specifically,  $R_j$  is the radius of an individual protrusion, idealized as a hemisphere. For instance, the class  $j = 1$  could consist of boulders with individual radii  $\sim R_1$ , while the class  $j = 2$  consists of cobbles with individual radii  $\sim R_2$ , and so forth. We use  $l_j$  to denote the distance between the centers of nearest neighbors in class  $j$ , and  $l_{e,j}$  for the span of the ice roof between nearest neighbors (which is generally less than  $l_j$ ). To be definite, we assume that the classes  $j$  are ordered by size, so that  $R_1 \gg R_2 \gg \dots \gg R_N$  and  $l_1 \gg l_2 \gg \dots \gg l_N$ .

Our next step is to calculate the downward ice velocity around bed protrusions of size  $j$ . To generalize equations (9) and (13), we note that effective pressure  $p_e = \sigma_i - p_w$  denotes the difference between a far-field normal stress  $\sigma_i$  (given by overburden in the case of a single protrusion size in equation (9)) and a pressure  $p_w$  at the ice roof between the supporting protrusions (given by water pressure in the case of a single protrusion size). For one protrusion size, the effective stress driving closure is equal to the effective pressure,  $\sigma_e = p_e$ . However, when there is more than one size class present, we can no longer identify the far-field stress with overburden because part of the overburden will be supported by protrusions of larger size classes. Additionally, smaller protrusion sizes will act to support the ice between larger protrusion sizes, so the average stress between large grains is not equal to the water pressure.

Instead, we define the an effective stress  $\sigma_{e,j}$  that drives viscous creep of ice between neighboring protrusions of class  $j$  as the difference between far-field stress  $\sigma_j$  acting on these protrusions and the normal stress  $p_j$  acting on the ice roof between the  $j$ th class protrusions. To compute these stresses, we can observe that the normal stress  $p_j$  is in fact the far-field stress that acts on protrusions of the next class  $j + 1$  of smaller protrusions, so  $p_j = \sigma_{j+1}$  and

$$\sigma_{e,j} = \sigma_j - \sigma_{j+1}. \quad (15)$$

Figure 2 illustrates this stress recursion for different values of  $H$ . This recursion relation can be seen as analogous to the stress partitioning between different bedrock obstacle sizes in the hard-bed sliding theories of *Lliboutry* [1979], *Fowler* [1987] and *Schoof* [2005]. It works for all but the smallest and largest size classes. For the largest size class  $j = 1$ , (15) still holds, but we need to define the stress condition  $\sigma_1 = \sigma_i$ , that is, far field stress for the largest size class is indeed overburden. Similarly, for the smallest size class  $j = N$ , the normal stress at the ice roof between protrusions of this size is water pressure  $\sigma_{N+1} = p_w$ .

Summing over  $j$  in (15) and using the conditions on  $\sigma_1$  and  $\sigma_{N+1}$  gives

$$\sum_{j=1}^N \sigma_{e,j} = p_e, \quad (16)$$

where  $p_e$  is the same effective pressure as before,  $p_e = \sigma_i - p_w$ . Given a stress partition between bed protrusions of different size classes of the form (16), downward ice motion past the  $j$ th size class is then given by generalized forms of (9) and (13),

$$v_j = v = \mathcal{A} |\sigma_{e,j}|^{n-1} \sigma_{e,j} l_{e,j} + \frac{\beta K}{\rho_i L r_j} \frac{S_{i,j}}{S_{s,j}} \sigma_{e,j}. \quad (17)$$

Here,  $l_{e,j}$  is the spacing between nearest contacts between ice and  $j$ th size bed protrusions, while  $r_j$  is the radius of each contact area between ice and an individual  $j$ th size protrusion (corresponding to  $l_e$  and  $r_e$  in the case of a single protrusion size class, respectively).  $S_{s,j}$  is the total contact area normal to ice motion of the  $j$ th size class with the ice (corresponding to  $S_s$  for a single obstacle size class), and  $S_{i,j} = S_i - \sum_{k=1}^{j-1} S_{s,k}$ .

In equation, we have assumed that the ice must move past all protrusions at the same rate  $v$  (i.e.,  $v_1 = \dots = v_N = v$ ). If this were not the case, then mass continuity for the ice could not be satisfied. In equation (17), any  $v_j$  can be replaced by a single downward velocity  $v$  that describes the closure of the water gap between ice and bed. At this point, suppose that we are given an overburden  $\sigma_i$ , a water pressure  $p_w$ , and the geometrical parameters  $l_{e,j}$ ,  $r_j$  and  $S_{s,j}$ , describing the size distribution of bed protrusions and the extent of their contact with the ice roof. We would like to calculate how the total effective pressure is partitioned among the different protrusion size classes, and how fast ice moves past them. The model as formulated allows us to do this when  $v = v_1 = \dots = v_N$  because we have as many equations as unknowns in (16) and (17) namely the  $\sigma_{e,j}$  and  $v$  variables (where  $j = 1, 2, \dots, N$ ). If each protrusion size had a different velocity such that there were  $N$   $v_j$ 's, then there would be  $2N$  unknowns and  $N + 1$  equations. The assumption of a single downward velocity renders the system of equations tractable.

The system of nonlinear equations given by (16) and (17) allows both the stress partitioning into the  $\sigma_{e,j}$ 's and the closure velocity  $v$  to be computed as a function of  $p_e$  and the geometrical parameters  $l_{e,j}$ ,  $r_j$ , and  $S_{s,j}$ . As we have pointed out, we are interested specifically in the dependence of  $v$  on the sheet thickness  $H$ , which enters into this calculation by determining the extent of ice–bed contact. In other words,  $H$  determines the smallest size class  $N$  that is still in contact with the ice roof as well as the roof span  $l_{e,j}$ , the contact areas  $S_{s,j}$  and the radii  $r_j$  of individual contacts between ice and bed protrusions. We consider these geometrical relationships next.

### 3.2. Geometry of contact areas

The small-scale geometry of the bed as well as the water depth govern the length scales  $l_{e,j}$  and  $r_j$  as well as the areal terms  $S_{i,j}$  and  $S_{s,j}$ . (The protrusions considered in our theory can be any type of bed roughness: sediment clasts or bedforms on an unlithified bed or on bedrock. For the purposes of constructing our theory, no distinction needs to be made between these. It is only important that the protrusion distribution is known as the water depth  $H$  increases or decreases. For fast water flow, it is possible that an unlithified bed could erode. We do not consider this case here because our goal is to understand how closure works without the added complication of a mobile bed.) Each of these quantities  $l_{e,j}$ ,  $r_j$ ,  $S_{i,j}$  and  $S_{s,j}$  also depends on the water depth because  $H$  determines the degree of protrusion submergence. Figure 3 illustrates the protrusion, ice, and water

sheet relationship. Water flows along an ice–bed gap, and bed protrusions are either partially or wholly submerged. Those that are large enough to penetrate the ice–bed gap partially support the ice, and therefore sheet thickness  $H$  also determines the smallest size class that still plays a role in determining roof closure velocity.

The  $j$ th size class consists of bed protrusions  $R_j$  spaced a distance  $l_j$  apart, and protruding above the datum  $H = 0$ . All size classes that remain in contact with the ice roof must then have  $R_j \geq H$ , while size classes with  $R_j < H$  are submerged in the water sheet. This implicitly determines the smallest size class  $N$  in the calculation above. Size classes with  $j \leq N$  bridge the water sheet, and the contact radius  $r_j$  with the ice roof can be computed from basic geometry as (see Fig. 3b,c)

$$r_j = \sqrt{R_j^2 - H^2}, \quad (18a)$$

so that an individual contact area between a protrusion of the  $j$ th size class and the bed becomes  $\pi r_j^2$ . In a square of the bed of side length  $l_j$ , there will be precisely one such contact, so

$$\frac{S_{s,j}}{S_i} = \frac{\pi r_j^2}{l_j^2}, \quad (18b)$$

and therefore the term  $S_{i,j}/S_{s,j}$  in equation (16) can be calculated as

$$\frac{S_{i,j}}{S_{s,j}} = \frac{S_i - \sum_{k=1}^{j-1} S_{s,k}}{S_{s,j}} = \frac{1 - \sum_{k=1}^{j-1} \frac{\pi r_k^2}{l_k^2}}{\frac{\pi r_j^2}{l_j^2}}. \quad (18c)$$

Lastly, the roof span between nearest neighbors is parameterized as

$$l_{e,j} = \sqrt{l_j^2 - \pi r_j^2}, \quad (18d)$$

so that  $l_{e,j}^2/l_j^2$  is the fraction of the ice area  $S_i$  not occupied by contacts with  $j$ th size protrusions.

Our model provides an internally consistent scaling to permit an understanding of closure by both closure and creep. Because our model does not solve a continuum mechanical formulation for ice roof closure, the quantities we calculate are presumably accurate to factors of  $O(1)$ . This model should, therefore, be understood as giving qualitatively correct behavior for the drainage system with correct orders of magnitude. However, even if our model did solve a continuum mechanical problem, the appropriate data for glacier bed geometries does not exist at present. As a result, a continuum formulation would probably not result in significant gains in accuracy. Thus, scalings such as ours provide the easiest means of understanding ice closure.

From equations (18), the geometrical parameters  $r_j$  and  $l_{e,j}$  in the model consisting of equations (16) and (17) can be related to sheet thickness  $H$  as well as the obstacle spacings and sizes  $l_j$  and  $R_j$ , allowing the sheet closure velocity  $v$  to be found as a function of effective pressure  $p_e$ , sheet thickness  $H$  and the fixed geometry of the bed protrusions determined by the  $l_j$  and  $R_j$  as well as the various material parameters in the model.

## 4. Computed closure rates

In this section, we compute several examples of closure rates of a subglacial water sheet as functions water depth and effective pressures, based on (16) and (17). We limit maximum effective pressure to approximately 0.9 MPa, equivalent to 100 m of ice overburden, and naturally consider only water depths  $H$  that are smaller than the maximum protrusion size  $R_1$  (as otherwise there would be no ice–bed contact).

Clearly, closure rates depend not only on  $H$ ,  $p_e$  and material parameters for ice, but also on the geometry of the bed, expressed in terms of the size and spacing parameters  $r_j$  and  $l_j$ . We begin by showing how creep and regelation act on a bed of uniform size protrusions that are equivalent in size to coarse sand. We then add a second grain size so that half of the grain area at the bed is covered by boulders and the other half is sand. In the final example, we construct a bed with multiple grain sizes that is intended to represent subglacial till, with protrusions ranging from boulders to clay-sized particles. Other grain distribution examples were treated by Creyts [2007, Chap. 3], and those results are compatible with results presented here. For all examples, we assume that grains maintain closest hexagonal packing on a flat plane. The cross-sectional area occupied by sediment grains is thus 91% of the total bed area. In other words, each of the examples has a bed area porosity of  $n_w \sim 0.09$ . By bed area porosity, we simply mean the fraction of bed, projected onto a plane parallel to the mean bed slope, that is not occupied by sediment grains. Nonuniform packing of spheres can yield bed area porosities space higher or lower than 0.09, but we keep this value to facilitate comparison among different examples.

#### 4.1. Uniform grain size example

An example of the downward motion of ice over a bed composed of uniform sand appears in Figure 4 with relevant parameters from Table 1. In this case, water depth is limited to  $R = 0.5$  mm with  $l$  about 0.9 mm. Here, black contours indicate closure velocity structure with the highest velocities occurring in the upper right. Using the recursion scheme, we reconstruct both regelation and creep velocity components. Overall, closure velocities are governed by regelation, and over 99% of the closure velocity is the regelation component. This is a result of a small grain size. The packing of grains does not have an effect on the closure mechanism. Even for wide sand spacing relative to grain radius, the creep length scale is too small to allow creep to be active. The downward slope of velocity contours with increasing effective pressure in Figure 4 is a result of higher stresses overcoming the effect of increasing total cross sectional area in equation (17). Most velocities lie in the range  $0-5 \times 10^{-6}$  m s $^{-1}$ . However, at the maximum elevation, where the contact area is small, velocities are over an order of magnitude higher. This response is true for all grain sizes. Regelation velocities also can increase by an order of magnitude by increasing grain spacing, because this increases the relative driving stress.

#### 4.2. Two grain size example

Figure 5 builds on the sand-sized case to include boulders. In this example, half of the bed is covered with boulders ( $R_1 = 0.256$  m,  $l_1 \simeq 0.674$  m) while the other half is sand ( $R_2 = 0.0005$  m,  $l_2 \simeq 0.001$  m). Both closure mechanisms are activated over different areas of  $p_e$ - $H$  space. When effective pressures are low, regelation is the dominant closure mechanism ( $v_r/v > 0.9$ ). Where effective pressures are relatively high, creep dominates ( $v_c/v > 0.9$ ). Between the regelation and creep regimes in Figure 5, there is a mixed regime, where both mechanisms are relevant. Where ice interacts with sand at the bottom of the figure, the regelation component increases. Because of the stress partitioning between sand and boulders, a mixed regime lies below the creep regime in Figure 5.

The velocity structure in Figure 5 is fairly subdued. Because we have assumed  $n = 3$  in the flow law, the velocity contours are spaced cubically in the creep regime along the right hand side of the figure. The curve of these lines results from effective length  $l_e$  decreasing with water depth. Velocity magnitudes are in the range  $0-2.5 \times 10^{-6}$  m s $^{-1}$ .

#### 4.3. Multiple grain sizes

In this example, we assume the sediment grain size distribution follows that of a deformation till. To obtain a grain

size distribution, we assume fractal scaling, and define  $N_{s,j}$  as the number density of the  $j$ th size class as

$$N_{s,j} := \frac{\pi R_j^2}{l_j^2} = N_0 \left( \frac{R_j}{R_0} \right)^{-a}, \quad (19)$$

where  $N_0$  is a reference number density and  $R_0$  is a reference grain size. Measurements on tills generally show that  $a \sim 2.9$  [Hooke and Iverson, 1995; Khatwa et al., 1999] but can be lower [e.g., Fischer and Hubbard, 1999]. Here we assume that the fractal index  $a = 3$ , which indicates that all measured grain sizes occupy roughly the same volume of the till.

In reality, grain sizes are continuous, but our theory is built around discrete size classes and is in that sense similar to the linked-cavity theory of Fowler [1987], which also represents bed protrusions in discrete size classes. To discretize grain sizes, we use the the  $\Phi$ -scale commonly used to classify loose sediments. In terms of grain radius  $R$ ,  $\Phi$  is defined as

$$R = 2^{-(\Phi+1)} \times 0.001 \text{ m}. \quad (20)$$

We construct grain size classes  $R_j$  by putting  $R_j = 2^{-(\Phi_j+1)} \times 0.001$  m with  $\Phi_j = -9, -8, \dots, 8$ . As a result, grain sizes are separated by a factor of two, and this may appear to contradict assumptions that  $R_1 \gg R_2 \gg \dots$  and  $l_1 \gg l_2 \gg \dots$ . These assumptions are necessary to separate the effects of different grain sizes in section 3.1. We are using the asymptotic limit of vanishing grain size ratios to approximate a bed with protrusions that have a fixed and finite size ratio. The question of when this limit becomes a good approximation is one that we cannot directly answer here, though we expect that our model will produce at least qualitatively the right behavior. Bluntly, as  $R_{j+1} \rightarrow R_j$ , the theory presented above breaks down. However, results discussed below using  $R_{j+1} = R_j/2$ , illustrate behavior that is qualitatively correct with plausible closure velocity magnitudes.

The largest size class is  $R_1 = 0.256$  m in the discrete grain size distribution described in (20), and our grain size distribution therefore includes coarse gravel, cobbles, and boulders. These larger grain sizes are undoubtedly present in deformation tills, which are one of the most common types of subglacial till [Benn and Evans, 1998, Chap. 10]. Grain sizes in deformation tills are likely indicative of protrusions along the bed. While there are various mechanistic interpretations of these tills, these are beyond the scope of this paper. Rather, we seek a reasonable distribution of material at the bed, and grain size data exists for deformation tills that has been interpreted via equation (20) [for an overview, see Clarke, 2005]. Sampling for these tills, however, is usually focused on smaller grains. Equivalent studies for rivers have shown that larger grains are not sampled adequately [e.g., Church et al., 1987], and this sampling problem likely exists for tills, so our chosen grain size distribution is therefore likely to be reasonable.

Results for this 18-grain-size distribution appear in Figure 6. Similar to the two-grain case, regelation-dominated closure ( $v_r/v > 0.9$ ) only occurs for low effective pressures. For higher effective pressures, creep-dominated closure ( $v_c/v > 0.9$ ) occurs for the largest grain size to a water depth of  $H = 0.128$  m. At this water depth, the second grain size ( $R_2$ ) begins to affect the closure velocity. For water depths shallower than 0.128 m but greater than about 0.09 m, the regelation length scale  $r_2$  is small, meaning that regelation velocities are relatively high (eq. (13)). In this

case, when water depths are smaller than but comparable to grain radii, equation (18a) states that the regelation length scale will be small. Regelation, therefore, plays a larger role in the total closure velocity, and the areas of creep-dominated closure are separated by a mixed closure regime.

At a water depth of 0.064 m, corresponding to contact with the third protrusion size  $R_3$ , a similar change from creep-dominated to mixed mode closure occurs because  $r_3$  is small and regelation velocities increase. Below a water depth of 0.064 m, no further creep-dominated closure appears in Figure 6 because the introduction of each successive grain size introduces an additional small  $r_j$ , and the regelation velocity increases relative to the total closure velocity.

Despite closure velocity magnitudes hovering again in the  $0\text{--}10 \times 10^{-6} \text{ m s}^{-1}$  range, the closure velocity structure is very different from the two grain example. In the upper creep-dominated regime, closure velocities are notably higher than in the creep regime in Figure 5. There are two reasons for this increase in velocity. Because there are more grain size classes in present in Figure 6, there is a smaller population density of the largest grains. The result is that more stress is focused on the larger grains for greater  $H$ . The second cause is that the largest creep length scale  $l_{e,1}$  is bigger because of the increase in number of grain sizes. The focusing of the stress on fewer contacts accounts for 2–3 times the velocity increase while the change in length scale accounts for 3–4 times the velocity increase. The closure velocities are higher by roughly an order of magnitude because of this concentration effect.

With more large grain sizes, we can also examine the stress partitioning. Figures 7 and 8 show the relative driving stresses on each grain. For low effective pressures,  $R_1$  requires proportionally more of the available stress (Fig. 7a). This requirement occurs because  $r_1$  is relatively large, making regelation slow, and the driving stress is low, making creep slow. Other grain sizes have faster regelation velocities at low driving stress. Stress must concentrate on the largest grains to increase the ice velocity past these grains so that continuity is satisfied. For higher effective pressures, fractional stress on grain size  $R_1$  decreases more rapidly with decreasing water depth than at lower effective pressures. This decreasing trend results from the power-law dependence of creep velocity on effective pressure. Closure velocities can then be high on  $R_1$  without requiring high stresses.

Smaller grain sizes follow trends similar to the larger grain sizes. Smaller grains have smaller  $r_j$ , and regelation occurs more readily ( $R_2$  to  $R_5$  in Figs. 7b–e and 8b–e). Higher effective pressures activate creep because it is power law dependent. However, creep only contributes significantly to the total closure velocity for  $R_1\text{--}R_4$ . For  $R_i \leq R_5 = 0.016 \text{ m}$ , regelation is always the dominant closure mechanism, and the smaller grains (*e.g.*, Fig. 7e,f, and 8e,f) support very little of the overall available driving stress. Grain sizes smaller than  $R_8 = 0.002 \text{ m}$  each support less than 1% of the available driving stress. Collectively, these 10 smaller grain sizes account for less than 2% of the entire stress partitioning. This result stems from the inverse dependence of regelation on  $r_j$  (eq. 13).

## 5. Water sheet dynamics

Armed with our description of ice roof closure, we can now address the dynamics of the water sheet itself, when modeled at horizontal length scales that are much larger than the obstacle spacings  $l_j$ . We consider only a simplified version of such a sheet model in order to address the question of sheet stability, and present a more complete theory in a separate paper. Specifically, as in section 2, we consider only the stability of the water sheet to transverse perturbations in sheet thickness  $H$ , assuming that the flow of water is unidirectional in the  $y$ -direction (so there is no transverse hydraulic gradient) and that  $H$  depends only on  $x$  and  $t$ .

We use the same notation as in section 2. With a Darcy-Weisbach friction law for water flow in the sheet, we can once again relate flow velocity in the  $y$ -direction to hydraulic gradient  $\partial\phi/\partial y$  and sheet thickness  $H$ :

$$u = -\sqrt{\frac{4H}{\rho_w f_d}} \left| \frac{\partial\phi}{\partial y} \right|^{-1/2} \frac{\partial\phi}{\partial y}. \quad (21)$$

Viscous dissipation in the water sheet will again lead to melting of the ice roof. Because we are interested in large horizontal length scales, we ignore turbulent diffusion and advection of heat in the sheet here (which are germane to smaller scales as considered in section 2), and assume that heat dissipated viscously causes local melting of the ice roof at rate  $m$ , so

$$mL = -Hu \frac{\partial\phi}{\partial y} = \frac{2H^{3/2} |\partial\phi/\partial y|^{3/2}}{\sqrt{\rho_w f_d}} - q_0, \quad (22)$$

where  $q_0$  is a background heat flux as before. In order to obtain a steady state sheet, this rate of melting must be offset by ice roof closure, which the theory in section 3 allows us to compute in the general form

$$v = v(p_e, H). \quad (23)$$

An analytical form for  $v$  is generally not available for multiple protrusion sizes; therefore it must be computed numerically. We note however that  $v$  normally increases with both  $p_e$  and  $H$ . Physically, the reasons for this behavior are obvious: greater effective pressure will accelerate the creep closure and regelation mechanisms, while a greater sheet thickness will lead to less contact between ice and bed and hence less resistance to ice roof subsidence.

The evolution of the sheet thickness can therefore be cast in the form

$$\frac{\partial H}{\partial t} = m(|\partial\phi/\partial y|, H) - v(p_e, H), \quad (24)$$

where we emphasize that  $m$  defined in equation (22) depends on the hydraulic gradient  $\partial\phi/\partial y$  and on sheet thickness  $H$ .

A stability analysis along the lines of section 2 is now straightforward. For a fixed effective pressure  $p_e$  and hydraulic gradient  $\partial\phi/\partial y$ , we have a steady state uniform sheet solution of the form given implicitly by the solution  $\bar{H}$  of

$$v(p_e, \bar{H}) = m(|\partial\phi/\partial y|, \bar{H}) \quad (25a)$$

with corresponding steady water flow velocity

$$\bar{u} = -\sqrt{\frac{4\bar{H}}{\rho_w f_d}} \left| \frac{\partial\phi}{\partial y} \right|^{-1/2} \frac{\partial\phi}{\partial y}. \quad (25b)$$

Once more, we look at harmonic perturbations of the form

$$H = \bar{H} + H' \exp(ikx + \omega t). \quad (25c)$$

where  $H'$  is small. It is now straightforward to see that  $\omega$  is determined simply by the linearized form of (24),

$$\omega H' = \left[ \frac{\partial m}{\partial H} \Big|_{H=\bar{H}} - \frac{\partial v}{\partial H} \Big|_{H=\bar{H}} \right] H', \quad (26)$$

which yields

$$\omega = \frac{\partial m}{\partial H} \Big|_{H=\bar{H}} - \frac{\partial v}{\partial H} \Big|_{H=\bar{H}}. \quad (27)$$

The sheet is stable if  $\omega$  is negative, that is, if

$$\left. \frac{\partial v}{\partial H} \right|_{H=\bar{H}} > \left. \frac{\partial m}{\partial H} \right|_{H=\bar{H}}. \quad (28)$$

As expected, the water sheet flow is viable if melt rate and roof closure balance, and if roof closure increases more sharply with increasing sheet thickness than melt rate does.

Graphically, this can be interpreted as follows. For fixed  $p_e$  and  $\partial\phi/\partial y$ ,  $m$  and  $v$  can be treated as functions of  $H$  alone, and steady sheet thicknesses correspond to points of intersection of their graphs (Fig. 9, using parameters from Table 1). The steady sheet solution is also stable if the curve representing  $v$  crosses the curve representing  $m$  from below, *i.e.*, if the slope of  $v$  against  $H$  is steeper than the slope of  $m$ . Figure 9 illustrates this stability graphically. For any stable solution, increasing water depth a small amount leads to a higher closure rate than melt rate, which reduces the water depth back to the stable solution. Similarly, if water depth is decreased a small amount from a stable solution, the melt rate is greater than the closure rate and the water depth increases.

### 5.1. Steady state water depth and flux

We now look at numerical computations of steady state sheet thicknesses given by equation (25a) for realistic parameter values and assess their stability based on the above criterion given by inequality (25a). Given these results, we can also consider the corresponding water flux  $\bar{u}\bar{H}$  that a subglacial water system carries for corresponding combinations of effective pressure and hydraulic gradient. We then compare these with realistic values for water flux.

Steady state sheet thickness  $\bar{H}$  is shown as a function of effective pressure  $p_e$  and hydraulic gradient  $|\partial\phi/\partial y|$  in Figure 10. For a given hydraulic gradient, a balance between melt and closure is possible only if effective pressures are not too high because closure velocities are too large otherwise. In terms of Figure 9, this would correspond to the closure curve lying everywhere above the melting curve. The only possible steady state in that case is the absence of a water sheet ( $\bar{H} = 0$ ), which we have not depicted. Hence, the surface  $\bar{H}(p_e, |\partial\phi/\partial y|)$  in Figure 10 is shown only for combinations of  $p_e$  and  $|\partial\phi/\partial y|$  for which  $\bar{H} > 0$ .

The most striking feature of Figure 10 is the stepped appearance of the surface  $\bar{H}(p_e, |\partial\phi/\partial y|)$ , which is in fact a generally multivalued surface. For a given combination of  $p_e$  and  $|\partial\phi/\partial y|$ , there can in general, be more than one steady state sheet thickness. On one hand, the ‘illuminated’, nearly horizontal plateaux correspond to sheet thicknesses  $\bar{H}$  close to one of the  $r_i$ , where closure velocity  $v(p_e, \bar{H})$  is very sensitive to small changes in sheet thickness (see also Figure 9). Because of this sensitive dependence on  $\bar{H}$ , a wide range of melt rates can be balanced by closure for very similar values of  $\bar{H}$ , and hence steady state values of  $\bar{H}$  are relatively insensitive to hydraulic gradients and effective pressures. Moreover, the sensitive dependence of closure on  $\bar{H}$  implies that these plateaux correspond to stable steady states: small increases in  $\bar{H}$  lead to much larger increases in closure than melt, stabilizing the sheet (see also Fig. 9). The darker, steep parts of the surface  $\bar{H}(p_e, |\partial\phi/\partial y|)$  in Figure 10, on the other hand, correspond to unstable solutions. These correspond to points of intersection of the melt and closure curves in Figure 9 where melt rate increases more rapidly with sheet thickness than closure rate does.

We note that the stepped appearance of Figure 10 is partly the result of grouping bed protrusions into discrete size classes. In this case, each of the plateaux corresponds to a different size class, and we optimistically infer that similar multiple solutions occur for a continuous distribution of size classes. To resolve this issue would require either a generalization to a continuous distribution of size classes, which

we defer to future work. However some tills have bimodal size distributions, for which a treatment using distinct size classes would be appropriate.

An important observation is that the stable branches of the surface  $\bar{H}(p_e, |\partial\phi/\partial y|)$  are those on which  $\bar{H}$  decreases with effective pressure. This is illustrated further in Figure 11, where  $\bar{H}$  is plotted as a multivalued function of  $p_e$  for various values of hydraulic gradient  $|\partial\phi/\partial y|$ . Clearly, the stable plateaux in Figure 10 correspond to the parts of these curves that are nearly flat but slope gently downward to the right (*i.e.*, on which  $\partial\bar{H}/\partial p_e < 0$ ), while the unstable branches of the surface in Figure 10 correspond to the parts of these curves that slope upward to the right. This feature can be derived from the stability criterion given by the inequality (28). Here, steady state sheet thicknesses are defined implicitly by equation (25a); differentiating and applying the chain rule gives

$$\frac{\partial v}{\partial p_e} + \frac{\partial v}{\partial H} \frac{\partial \bar{H}}{\partial p_e} = \frac{\partial m}{\partial H} \frac{\partial \bar{H}}{\partial p_e}, \quad (29a)$$

so

$$\frac{\partial \bar{H}}{\partial p_e} = - \frac{\partial v}{\partial p_e} / \left[ \frac{\partial v}{\partial H} - \frac{\partial m}{\partial H} \right]. \quad (29b)$$

If closure velocity  $v$  increases with effective pressure  $p_e$  and the stability criterion (28) is satisfied, it follows that  $\partial\bar{H}/\partial p_e < 0$ . Thus, stable, steady state sheet thicknesses decrease with increasing effective pressure, and the sheet stores less water at higher effective pressure, as may be expected intuitively for a distributed water system. If this were not the case, an area where the sheet is thicker would have a higher effective pressure than where the sheet is thinner. Thus water would be drawn away from the thinner area, which would cause water to concentrate into the thickened areas. The net result would be channelization. This observation, while not captured by our simple description of sheet dynamics in section 5, becomes relevant when that description is extended to include spatial variations in effective pressure.

Up to this point, we have looked only at water depth variations. In turn, width-averaged water flux is simply  $Q = \bar{u}\bar{H}$  for a sheet that is in steady state. Because discharge can also be expressed as functions of effective pressure and hydraulic gradient, we can plot the dependence of  $Q$  in Figure 12. Again, the surface depicting water flux has a stepped appearance, which is due to the same physics as the stepped appearance of Figure 10, and ‘illuminated’ parts of the surface again correspond to stable solutions. Notably, these stable branches of the surface have discharge increasing with hydraulic gradient and increasing with effective pressure. Water discharge that increases with hydraulic gradient is expected for a distributed drainage system, while the dependence on effective pressure is simply the result of water depth controlling the hydraulic conductivity.

## 6. Discussion

The existence of multiple steady states for distributed water sheets with depth greater than the laminar–turbulent transition ( $\approx 3$  cm for our parameter choices) suggests that a given combination of effective pressure and hydraulic gradient may correspond to a number of different drainage configurations. Abrupt switches could then occur, between, say, a relatively inefficient and a more efficient drainage system as effective pressure and hydraulic gradient are changed (*i.e.*, one with low  $\bar{H}$  and one with high  $\bar{H}$ ). This behavior is fundamentally different from channelized turbulent flows [*e.g.*, R othlisberger, 1972; Shreve, 1972] where flux can only increase as a monotonic function of the hydraulic potential

gradient and effective pressure. These multiple steady states are a result of the closure scheme presented in section 3, and relies on a distribution of protrusions which is such that ice closure depends sensitively on sheet thickness for certain values of  $\bar{H}$ , where an increase in sheet thickness leads to loss of contact with a dominant protrusion size. We have shown this to be plausible for discrete size classes; while for a real bed, the distribution of protrusion sizes may be smoother than that assumed above. *Creyts* [2007] showed that the rates of closure are qualitatively similar for grain size distributions with more size classes. For these, the changes in closure velocity are more subdued, but they may still lead to closure velocity depending sensitively on sheet thickness around certain values of  $\bar{H}$ . We thus expect multiple steady states for more general distributions of protrusion sizes [*e.g.*, *Benoist*, 1979; *Hubbard et al.*, 2000] but leave this extension for future work.

We have not addressed two-dimensional effects mathematically. For distributed sheets, lateral flow of water will be important: relatively underpressured regions of the bed will draw water, and relatively overpressured regions will expel water. For regions with extents on the order of an ice thickness or larger, we expect changes in effective pressure to progress in a diffusive manner; and because our model is mathematically local (*i.e.*, no spatial coupling), these regional effects are not developed. A significant complication however lies in the possibility of multiple steady states and of switches between them, which could conceivably lead to oscillatory behavior in drainage.

Furthermore, for low water flows that are laminar rather than turbulent (with Reynolds number  $\text{Re} < 2300$ ), our argument in section 2 is not applicable. Because we cannot make an argument for enhanced heat transfer perpendicular to flow, we expect channelization to occur as described by *Walder* [1982], albeit rather slowly. However, our stability argument from section 2 holds where flow is turbulent above a specific discharge of approximately  $4 \times 10^{-3} \text{ m}^3 \text{ s}^{-1} \text{ m}^{-1}$  (Fig. 12). This corresponds to a few centimeters ( $\simeq 3$ ) of sheet thickness, depending on hydraulic gradient.

The analysis presented here is broadly consistent with observed ice stream hydrology. Recent work on the hydraulics of ice streams have shown that water is areally distributed with temporal changes between states of deep and shallow water [*e.g.*, *Fricker et al.*, 2007]. Hydraulic potential gradients are within the range 0–20 Pa  $\text{m}^{-1}$ , and it is possible that multiple steady states of the hydraulic system exist here, which can be captured by our theory. One additional complication that is likely to be relevant in ice streams is the effect of sliding on the closure velocity  $v$ : sliding can conceivably lead to ice being pushed upward as it moves over bed protrusions, which will locally reduce the closure velocity. Parts of the water sheet may then function somewhat like water-filled cavities, in the sense that the sheet is prevented from closing not by melting but by ice motion around bed protrusions [*Fowler*, 1986, 1987; *Kamb*, 1987; *Walder*, 1986; *Schoof*, 2005]. Steady-state sheet thickness is then likely to depend not only effective pressure  $p_e$  and hydraulic gradient  $|\partial\phi/\partial y|$ , but also on sliding velocity, with sheet thickness increasing with sliding velocity [*e.g.*, *Schoof*, 2005].

Another question we have not addressed is the transition from flow in a water sheet to the formation of R-channels. Ultimately, this has to be driven by *Walder's* [1982] instability, which we have argued can be suppressed by a combination of diffusion of heat in the water sheet and the sliding of ice, which suppresses the unstable thickening of parts of the sheet as they move over bed protrusions (see section 2). However, it can be seen from the constraint (8) that this is only plausible for relatively small hydraulic gradients: at high hydraulic gradients, the rate of viscous dissipation in the water sheet is high enough that unstable thickening can

no longer be suppressed, and channelization must ensue. In terms of the surfaces in figures 10 and 12, this implies that the ‘stable’, stepped parts of these surfaces are in fact only stable for sufficiently low values of  $|\partial\phi/\partial y|$ , and in particular, that the topmost step is in fact unstable to channelization for large enough hydraulic gradients. In other words, we expect that there is a boundary on this topmost plateau that separates a part of it at low  $|\partial\phi/\partial y|$  that is stable to channelization from another part at high  $|\partial\phi/\partial y|$  that is unstable to channelization in the way described by *Walder* [1982]. However, the precise location of this boundary cannot be calculated from our theory.

## 7. Conclusions

Here, we have extended previous work [*e.g.*, *Walder*, 1982; *Weertman*, 1972] to show that distributed water sheets can be stable to much greater depth than previously quantified. The presence of protrusions that bridge the ice–bed gap can stabilize distributed sheets. Stabilization occurs because areas of greater water depth (and therefore those areas that are actively increasing water depth due to ice melt from enhanced viscous dissipation) can be offset by enhanced downward closure of an ice roof. This mechanism relies on a finite difference between overburden and water pressure (*i.e.*, a finite effective pressure) driving downward closure. This feature stands in contrast to water films without bed protrusions *Walder* [*e.g.*, 1982] where only water pressure balances ice overburden.

In constructing our theory, we have developed a recursive formulation for computing the partition of stresses between different protrusion sizes that exist at the bed and related these stresses to the downward motion of the ice through both viscous creep and regelation mechanisms. As a result, we are able to relate the closure velocity of the ice roof above the water sheet to effective pressure and sheet thickness. A steady state water sheet can then be formed if the melt rate of the ice roof due to viscous dissipation in the sheet balances the closure velocity. Steady state sheets of this form can, however, only persist if they are also *stable*, that is, if a small departure from steady state thickness leads to a negative feedback that returns thickness to its steady state value. This requires that a small thickening of the sheet from steady state should lead to a larger increase in downward ice velocity than the corresponding increase in melt rate. In turn, this is the case if a thickening of the sheet leads to a significant loss of contact between ice and bed protrusions.

Our theory predicts that such stable steady states do exist, and in fact, for beds with multiple protrusion sizes, multiple stable steady states can exist. Switches between these steady states can then lead to abrupt switches in water discharge in the drainage system. Future work will extend our theory to take account of spatial variations in effective pressure and hydraulic gradient, and to understand the effects of potential hydraulic switches.

## Notation

$a$	fractal index.
$A$	Ice creep coefficient.
$c$	ice specific heat at constant pressure.
$f_d$	Darcy-Weisbach friction factor.
$H$	water depth (= sheet thickness = storage).
$j, k$	indicate protrusion size, class dependence (as subscript).
$k$	wavenumber.
$K$	thermal conductivity.
$l$	protrusion spacing.
$l_e$	effective creep length scale.
$L$	ice latent heat.
$m$	melt rate.
$n$	index from Glen's flow law.
$N_s$	number of grains.
$N_0$	reference number of grains.
$p_w$	subglacial water pressure.
$p_e$	total effective pressure.
$q_0$	heat flux.
$Q$	width-averaged subglacial water flux.
$r$	water depth dependent protrusion contact radius.
$r_e$	regelation length scale.
$R$	protrusion (grain) radius.
$R_0$	reference grain radius.
$S_i$	ice area.
$S_w$	water area.
$S_s$	ice-bed contact area.
$t$	time.
$T$	water temperature.
$T_m$	ice melting temperature.
$u$	water velocity.
$u_b$	ice sliding velocity.
$v$	total closure velocity.
$v_c$	creep closure velocity.
$v_r$	regelation closure velocity.
$x$	axis perpendicular to flow.
$y$	axis along flow.
$\beta$	pressure melting parameter.
$\kappa$	turbulent diffusivity in water.
$\rho_w$	water mass density.
$\rho_i$	ice mass density.
$\sigma$	stress.
$\sigma_e$	effective stress.
$\sigma_i$	ice overburden stress.
$\sigma_s$	stress on bed contact area.
$\phi$	hydraulic potential driving flow.
$\Phi$	sediment grain size index.
$\omega$	growth rate.

**Acknowledgments.** TTC was funded by NSERC's Climate System History and Dynamics program, the University of British Columbia, and an US NSF Office of Polar Programs Postdoctoral Fellowship. CGS was funded by a Canada Research Chair, by NSERC Discovery Grant no. 357193-08, by the Canadian Foundation for Climate and Atmospheric Science through the Polar Climate Stability Network, and by US NSF grant no. DMS-03227943. We thank G.K.C. Clarke and H. Björnsson for stimulating discussions and R.B. Alley for comments on an early version of this manuscript. J. Walder and an anonymous reviewer are gratefully acknowledged for comments that improved

the manuscript. We also thank P.E. Creyts for useful discussions on conceptual figures.

## References

- Benn, D. I., and D. J. A. Evans (1998), *Glaciers and glaciation*, Arnold, London.
- Benoist, J.-P. (1979), The spectral power density and shadowing function of a glacial microrelief at the decimetre scale, *J. Glaciol.*, *23*(89), 255–267.
- Björnsson, H. (2002), Subglacial lakes and jökulhlaups in Iceland, *Global Planet. Change*, *35*, 255–271.
- Church, M. A., D. G. McLean, and J. F. Wolcott (1987), River bed gravels: sampling and analysis, in *Sediment transport in gravel-bed rivers*, edited by C. R. Thorne, J. C. Bathurst, and R. D. Hey, pp. 43–88, John Wiley, Hoboken, N.J.
- Clarke, G. K. C. (2003), Hydraulics of subglacial outburst floods: new insights from the Spring-Hutter formulation, *J. Glaciol.*, *49*(165), 299–313.
- Clarke, G. K. C. (2005), Subglacial processes, *Annu. Rev. Earth Planet. Sci.*, *33*, 247–276, doi: 10.1246/annrev.earth.33.092203.122621.
- Creyts, T. T. (2007), A numerical model of glaciohydraulic supercooling: thermodynamics and sediment entrainment, Ph.D. thesis, Univ. of B.C., Vancouver, B.C., Canada.
- Emerson, L. F., and A. W. Rempel (2007), Thresholds in the sliding resistance of simulated basal ice, *The Cryosphere*, *1*(1), 11–19.
- Fischer, U. H., and B. Hubbard (1999), Subglacial sediment textures: character and evolution at Haut Glacier d'Arolla, Switzerland, *Ann. Glaciol.*, *28*, 241–246.
- Fountain, A. G., and J. S. Walder (1998), Water flow through glaciers, *Rev. Geophys.*, *36*(3), 299–328.
- Fowler, A. C. (1981), A theoretical treatment of the sliding of glaciers in the absence of cavitation, *Phil. Trans. R. Soc. Lond.*, *298*(1445), 637–685.
- Fowler, A. C. (1986), A sliding law for glaciers of constant viscosity in the presence of subglacial cavitation, *Proc. Roy. Soc. Lond. A*, *407*, 147–170.
- Fowler, A. C. (1987), Sliding with cavity formation, *J. Glaciol.*, *33*(115), 255–267.
- Fricker, H. A., T. Scambos, R. Bindshadler, and L. Padman (2007), An active subglacial water system in West Antarctica mapped from space, *Science*, *315*, 1544–1548, doi: 10.1126/science.1136897.
- Hooke, R. L., and N. R. Iverson (1995), Grain-size distribution in deforming subglacial tills: role of grain fracture, *Geology*, *23*(1), 57–60.
- Hubbard, B., and P. Nienow (1997), Alpine subglacial hydrology, *Quaternary Sci. Rev.*, *16*, 939–955.
- Hubbard, B., M. J. Siegert, and D. McCarroll (2000), Spectral roughness of glaciated bedrock geomorphic surfaces: implications for glacier sliding, *J. Geophys. Res.*, *105*(B9), 21,295–21,303.
- Jóhannesson, T. (2002), Propagation of a subglacial flood wave during the initiation of a jökulhlaup, *Hydrolog. Sci. J.*, *47*(3), 417–434.
- Kamb, B. (1987), Glacier surge mechanism based on linked cavity configuration of the basal water conduit system, *J. Geophys. Res.*, *92*(B9), 9083–9100.
- Kamb, B. (2001), Basal zone of the West Antarctic ice streams and its role in lubrication of their rapid motion, in *The West Antarctic Ice Sheet: behavior and environment, Antarctic Research Series*, vol. 77, edited by R. B. Alley and R. A. Bindshadler, pp. 157–199, American Geophysical Union, Washington, DC.
- Khatwa, A., J. K. Hart, and A. J. Payne (1999), Grain textural analysis across a range of glacial facies, *Ann. Glaciol.*, *28*, 111–117.
- Lliboutry, L. (1979), Local friction laws for glaciers: a critical review and new opinions, *J. Glaciol.*, *23*(89), 67–95.
- Magnússon, E., H. Rott, H. Björnsson, and F. Pálsson (2007), The impact of jökulhlaups on basal sliding observed by SAR interferometry on Vatnajökull, Iceland, *J. Glaciol.*, *53*(181), 50–58.

Murray, T., and G. K. C. Clarke (1995), Black-box modeling of the subglacial water system, *J. Geophys. Res.*, *100*(B7), 10,231–10,245.

Ng, F. S. L. (1998), Mathematical modelling of subglacial drainage and erosion, Ph.D. thesis, Oxford Univ., Oxford, U.K.

Nye, J. F. (1953), The flow law of ice from measurements in glacier tunnels, laboratory experiments and the Jungfraufirn, *Proc. Roy. Soc. Lond. A Mat.*, *219*, 477–489.

Nye, J. F. (1967), Theory of regelation, *Philos. Mag.*, *16*(144), 1249–1266.

Paterson, W. S. B. (1994), *The physics of glaciers*, 3rd ed., Pergamon, Tarrytown, NY.

Rempel, A. W. (2008), A theory for ice–till interaction and sediment entrainment beneath glaciers, *J. Geophys. Res.*, *113*(F1), F01,013, doi:10.1029/2007JF000870.

Röthlisberger, H. (1972), Water pressure in intra- and subglacial channels, *J. Glaciol.*, *11*, 177–203.

Röthlisberger, H., and H. Lang (1987), Glacial hydrology, in *Glacio-fluvial sediment transfer: an alpine perspective*, edited by A. M. Gurnell and M. J. Clark, pp. 207–284, John Wiley and Sons, New York.

Schlichting, H. (1979), *Boundary Layer Theory*, 7th ed., McGraw-Hill, New York.

Schoof, C. (2005), The effect of cavitation on glacier sliding, *Proc. Roy. Soc. Lond. A Mat.*, *461*, 609–627.

Shreve, R. L. (1972), Movement of water in glaciers, *J. Glaciol.*, *11*(62), 205–214.

Stone, D. B., and G. K. C. Clarke (1993), Estimation of subglacial hydraulic properties from induced changes in basal water pressure: a theoretical framework for borehole–response tests, *J. Glaciol.*, *39*(132), 327–340.

Wagner, W., A. Saul, and A. Pruß(1994), International equations for the pressure along the melting and along the sublimation curve of ordinary water substance, *J. Phys. Chem. Ref. Data*, *23*(3), 515–525.

Walder, J. (1982), Stability of sheet flow of water beneath temperate glaciers and implications for glacier sliding, *J. Glaciol.*, *28*(99), 273–293.

Walder, J. S. (1986), Hydraulics of subglacial cavities, *J. Glaciol.*, *32*(112), 439–445.

Walder, J. S., and A. Fowler (1994), Channelized subglacial drainage over a deformable bed, *J. Glaciol.*, *40*(134), 3–15.

Weertman, J. (1957), On the sliding of glaciers, *J. Glaciol.*, *3*(21), 33–38.

Weertman, J. (1972), General theory of water flow at the base of a glacier or ice sheet, *Rev. Geophys. Space*, *10*(1), 287–333.

Timothy T. Creyts, Department of Earth and Planetary Science, University of California, Berkeley, 307 McCone Hall, Berkeley, CA 94720-4767, USA. (tcreyts@berkeley.edu)

Christian G. Schoof, Department of Earth and Ocean Sciences, University of British Columbia, Vancouver, BC, V6T 1Z4, Canada

## Appendix A: Temperate versus subtemperate regelation

In the context of a theory for the freeze-on of subglacial sediments, Rempel [2008] studied contacts between glacial ice and bed particles not dissimilar from those considered above, and it is therefore relevant to compare the two theories and point out where they depart from one another.

One way to demonstrate that our essentially temperate regelation model is appropriate is to compute the thickness of the microscopic water film thickness that must separate bed protrusions from the overlying ice. The theory of interfacial premelting then allows this film thickness to be related to the temperature of the film [Emerson and Rempel, 2007; Rempel, 2008], and if it differs only insignificantly from the

melting point, then regelation is temperate. Film thickness can be estimated by calculating the water flux carried by this film in evacuating melt generated at the top of the protrusion. This flux can in turn be related to film thickness, water viscosity and the pressure gradient available to drive the flux as in appendix B of Emerson and Rempel [2007].

Here we wish to dwell a little further on the difference between our temperate regelation model and the theory in Rempel [2008]. In essence, the differences between the theories arises because there is no macroscopic subglacial water sheet in Rempel’s work, even when there is no frozen fringe. Ice penetrates directly into pore throats between the sediment grains that make up the glacier bed, and the corresponding high curvature of the ice–porewater interface plays an important role in supporting ice overburden. By contrast, surface tension effects do not play a role in force balance in our theory. Associated with the high curvature in Rempel’s theory is a dip in ice–porewater interface temperature below the pressure melting point  $T_m$  at which a flat ice–water interface would be stable. Consequently, the contact between ice and sediment grains is subtemperate at a temperature  $T_i$ , which allows the thickness of a premelted water film (of much smaller thickness than the pore throat radius) between ice and sediment grains to be estimated.

A downward regelation velocity  $v_r$  requires water melted at the ice–sediment contacts to be evacuated through this premelted film, and standard lubrication theory allows Rempel [2008, appendix A] to estimate the corresponding pressure difference that drives the required water flux. This pressure difference corresponds to our  $\Delta\sigma$  in equation (10), and, in the absence of a frozen fringe, to  $\delta p$  in Rempel’s theory.

The difference in our theory is that our macroscopic water sheet implies essentially zero curvature of the ice–water sheet interface, which therefore remains at the melting point  $T_m$ , and hence our theory deals with temperate regelation. Specifically, we do not know a priori the temperate  $T_i$  of the microscopic water film at ice–sediment particles, and the thickness of the film can therefore vary to accommodate the necessary water flux required by the regelation velocity  $v_r$ . Instead, we relate the rate of melting and refreezing around ice–sediment contacts to the heat flux associated differences in pressure melting point induced by pressure variations around the ice–sediment contacts [see also Fowler, 1981; Weertman, 1957]. This assumes that the ice–sediment contacts remain at the local pressure melting point, and is where our theory departs from that of Rempel [2008]. In Rempel’s theory, steady state without a frozen fringe implies the curvature  $\mathcal{K}$  in the pore throats must take the value required for surface tension to support the overburden. This curvature can in turn be related to the temperature at the base of the ice through the Clapeyron equation and the Gibbs–Thomson effect, and the corresponding temperature is generally below the melting point.

However, Rempel’s theory is still relevant to our work. Specifically, our numerical results predict a non-zero ice roof closure velocity even as sheet thickness  $H \rightarrow 0$ . Of course, once the macroscopic water sheet has disappeared and  $H = 0$ , ice does invade pore throats between sediment grains. This can be expected to suppress further downward motion (so  $v$  in our theory must effectively be discontinuous at  $H = 0$ ). In fact, once there is no macroscopic water layer, it is the theory in Rempel [2008] that predicts whether there is any further downward motion of ice into the substrate, and if so, at what rate.

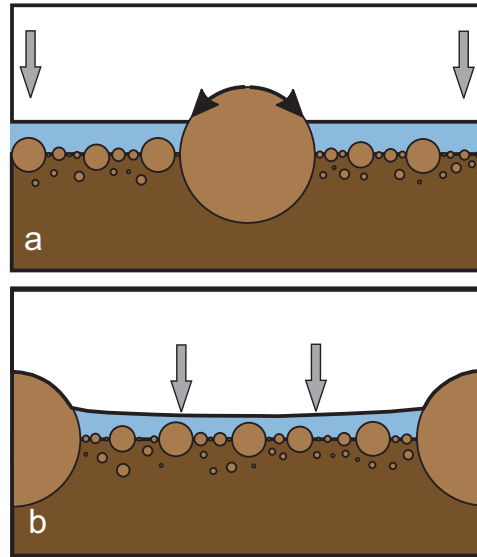


**Figure 1.** (a) A simple illustration of regelation closure. The water layer is the lightest gray. As the ice descends onto the grains, stress from the overlying ice is concentrated, and the ice melts. Grey arrows show the sense of ice motion. Black arrows indicate motion of water generated from ice melt. (b) An illustration of creep closure. Ice preferentially sags into the water layer with a larger spacing between particles.

**Table 1.** Model parameters.

Parameter	Value	Units	Notes
$\mathcal{A}$	$6.8 \times 10^{-24}$	$\text{s}^{-1} \text{Pa}^{-n}$	Creep coefficient [ <i>Paterson, 1994, p. 97</i> ]
$c$	4218	$\text{J kg}^{-1} \text{K}^{-1}$	Ice specific heat
$f_d$	0.12		Darcy-Weisbach friction coefficient [ <i>Clarke, 2003</i> ]
$g$	9.81	$\text{m s}^{-2}$	Gravitational acceleration
$K$	3.3	$\text{W m}^{-1} \text{K}^{-1}$	Thermal conductivity of ice or sediment
$L$	$3.336 \times 10^5$	$\text{J kg}^{-1}$	Latent heat of ice
$n$	3.0		Flow law index [ <i>Nye, 1953; Paterson, 1994</i> ]
$\beta$	$7.440 \times 10^{-8}$	$\text{K Pa}^{-1}$	Pressure melting coefficient [ <i>e.g., R�othlisberger and Lang, 1987</i> ]
$\rho_i$	916.7	$\text{kg m}^{-3}$	Ice mass density
$\rho_w$	1000.0	$\text{kg m}^{-3}$	Water mass density

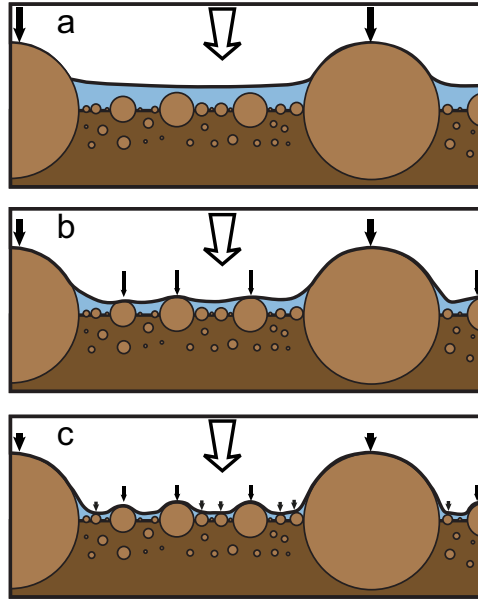


**Figure 2.** A simple illustration of the stress recursion scheme. Large white arrow in center represents ice overburden stress and is constant for a, b, and c. Water pressure is constant for all panels. Same color scheme for ice, water, and protrusions as Figure 1. (a) Black arrows at the top of large protrusions illustrate that stress divides evenly between the largest protrusions. (b) For smaller  $H$ , where ice is supported by a second size class, stress on largest protrusions lessens. Smaller protrusions support the remainder of the normal stress. (c) For an even smaller  $H$ , stress on largest protrusion sizes is smaller. Stress on the intermediate protrusion size also decreases because smallest protrusions bear some of the total stress available for closure.

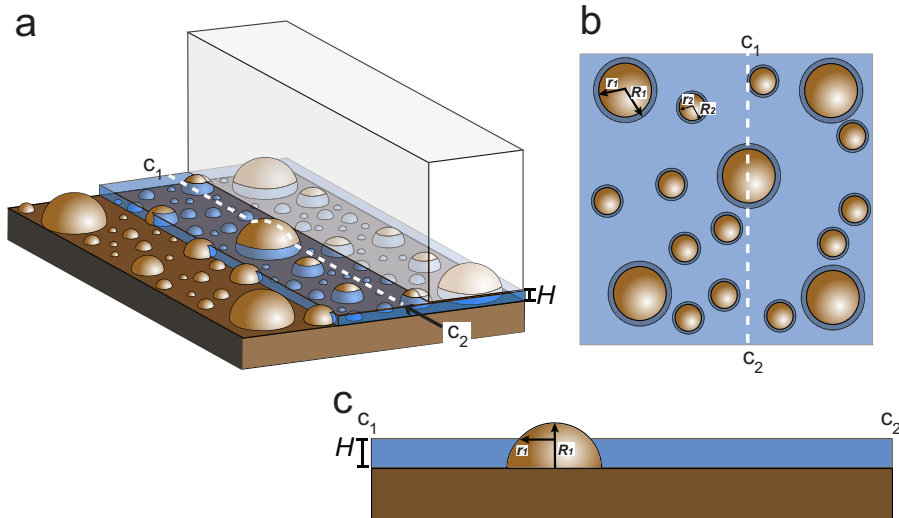


**Figure 3.** (a) Cut away view of glacier bed. Only the largest protrusion sizes and water support the ice. Water flows between an ice-bed gap. (b) Same as (a), but viewed from above. Only protrusions that support the ice are included. Protrusions with radius smaller than  $R_2$  are wholly submerged. Not to scale. (c) Cross section along  $c_1$  to  $c_2$  from (a) and (b) showing  $R_1$  and  $r_1$ .

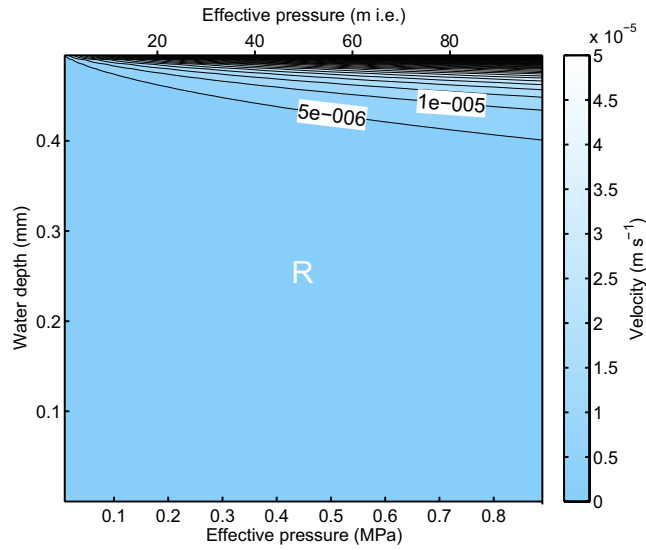


**Figure 4.** Closure rate as a function of water depth and effective pressure in meters of ice equivalent for a grain size of  $R = 0.5$  mm. Approximately 97.5% of values fall within the color scale. Higher values occur for small  $r$  where smaller areas of the grains are in contact with ice. Maximum downward velocity is about  $5.5 \times 10^{-4} \text{ m s}^{-1}$  for effective pressures of 100 m ice equivalent and as  $R$  tends to 0.5 mm. Black contour interval is  $5 \times 10^{-6} \text{ m s}^{-1}$ .

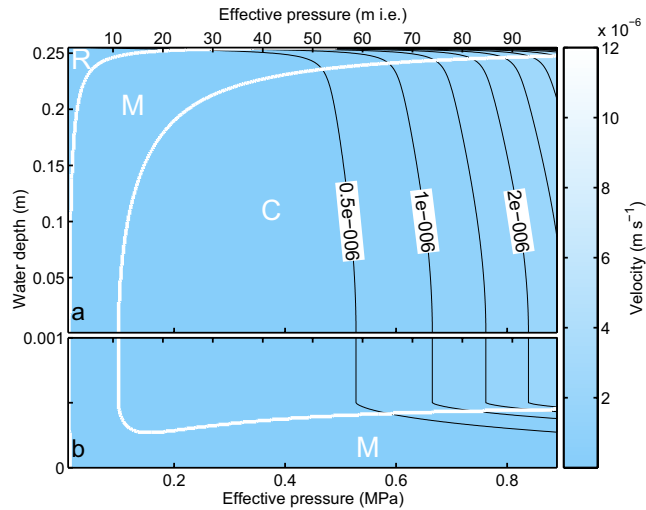


**Figure 5.** Closure rate as a function of water depth and effective pressure in meters of ice equivalent for two grain sizes of  $R = 0.256$  m and  $R = 0.0005$  m. Black contour interval is  $0.5 \times 10^{-6} \text{ m s}^{-1}$ . Large white letters and contours delineate areas of regelation-dominated closure (R), mixed mode closure (M), and creep-dominated closure (C). (a) Region from  $H = 0.001$  m to 0.256 m. (b) Region from  $H = 0.0$  m to 0.001 m.

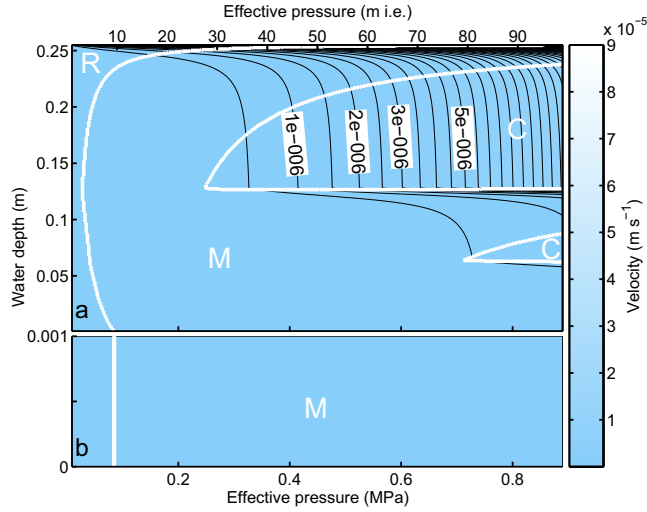


**Figure 6.** Closure rate as a function of water depth and effective pressure in meters of ice equivalent for 18 grain sizes from  $\Phi = -9$  to  $\Phi = 8$  m (see text for details). Black contour interval is  $0.5 \times 10^{-6} \text{ m s}^{-1}$ . Large white letters and contours delineate areas of regelation-dominated closure (R), mixed mode closure (M), and creep-dominated closure (C). (a) Region for water depth  $H = 0.001$  m to  $0.256$  m. (b) Region from for water depth  $H = 0.0$  m to  $0.001$  m.

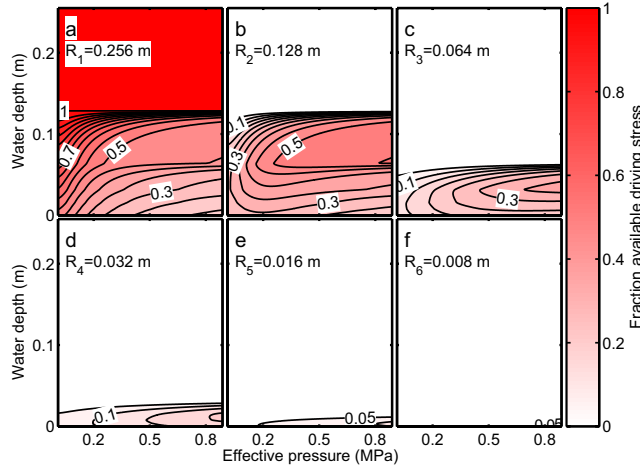


**Figure 7.** Stress partitioning via the recursion scheme for the closure velocity in Figure 6. Total stress on each grain size can be computed by multiplying the contour value multiplied with the horizontal axis value. Contour for fractional driving stress interval is 0.05. (a) For  $R_1 = 0.256$  m (b) For  $R_2 = 0.128$  m (c) For  $R_3 = 0.064$  m (d) For  $R_4 = 0.032$  m (e) For  $R_5 = 0.016$  m (f) For  $R_6 = 0.008$  m.

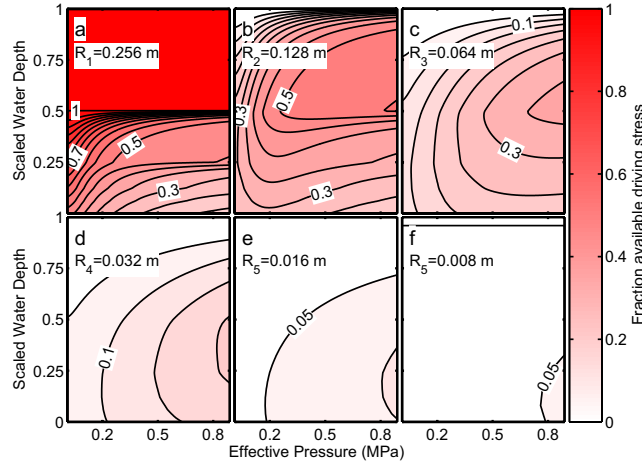


**Figure 8.** Figure 7 rescaled to the height of the individual protrusion size. The dimensional vertical axis is recovered by multiplying the vertical axis by the protrusion size. Contour interval for fractional driving stress is 0.05. (a) For  $R_1 = 0.256$  m. (b) For  $R_2 = 0.128$  m (c) For  $R_3 = 0.064$  m (d) For  $R_4 = 0.032$  m (e) For  $R_5 = 0.016$  m (f) For  $R_6 = 0.008$  m.

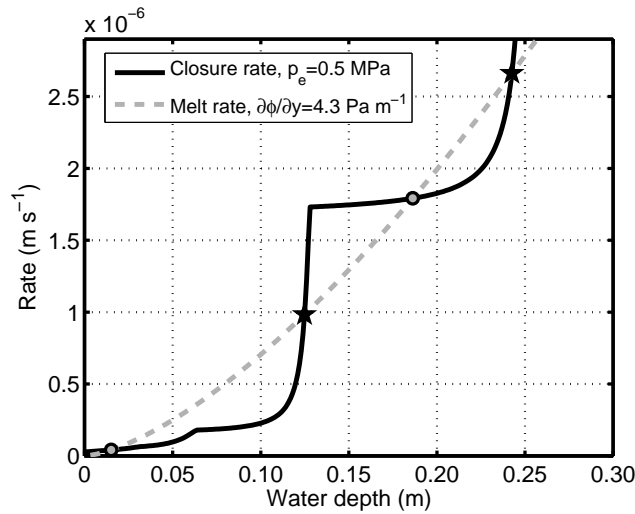


**Figure 9.** Example of a solution plot. Solutions exist where both rates intersect as a function of water depth ( $H$ ) for fixed effective pressure and hydraulic gradient. Black stars represent stable solutions. Grey circles are unstable solutions.

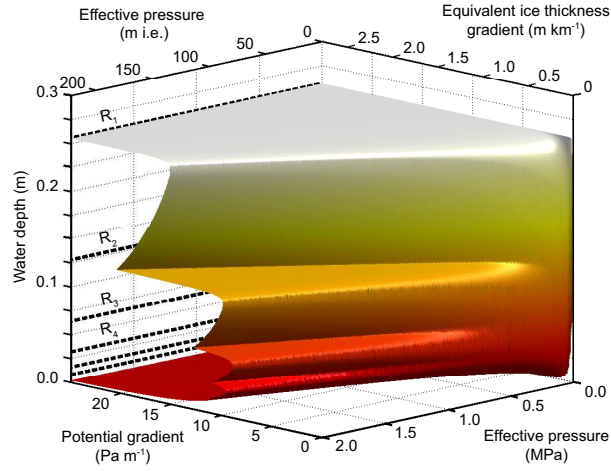


**Figure 10.** Steady state water depth  $\bar{H}(p_e, |\partial\phi/\partial y|)$  plotted against  $p_e$  and  $|\partial\phi/\partial y|$ . Illumination is from the upper right. Note that  $\bar{H}$  is generally multi-valued. Stable branches of  $\bar{H}$  are the broad plateaux with high reflectance and correspond to water sheet thickness close to the protrusion sizes  $R_i$ . Unstable solutions are shaded and slope into the page. The trivial stable solution of  $\bar{H} = 0$  is not plotted.

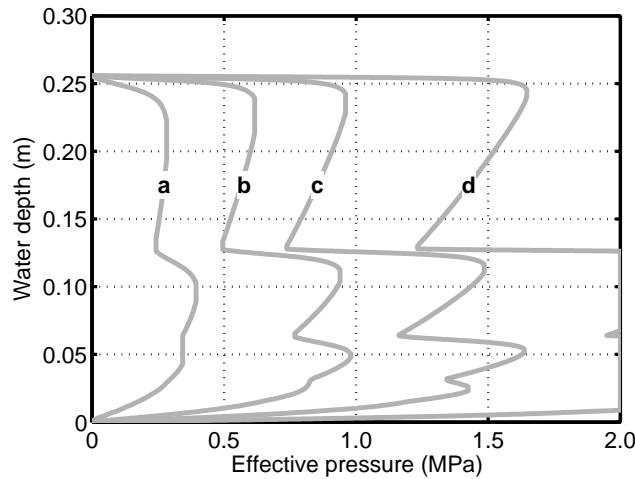


**Figure 11.** Steady state water depth  $\bar{H}(p_e, |\partial\phi/\partial y|)$  as a function of effective pressure for constant values of hydraulic potential gradient. Solutions that slope downward to the right (*i.e.*, with  $\partial\bar{H}/\partial p_e < 0$ ) are stable. Those that slope to the left are unstable. Lines correspond to (a)  $\partial\phi/\partial y = 2.5 \text{ Pa m}^{-1}$ , (b)  $\partial\phi/\partial y = 5.0 \text{ Pa m}^{-1}$ , (c)  $\partial\phi/\partial y = 7.5 \text{ Pa m}^{-1}$ , (d)  $\partial\phi/\partial y = 12.5 \text{ Pa m}^{-1}$ .

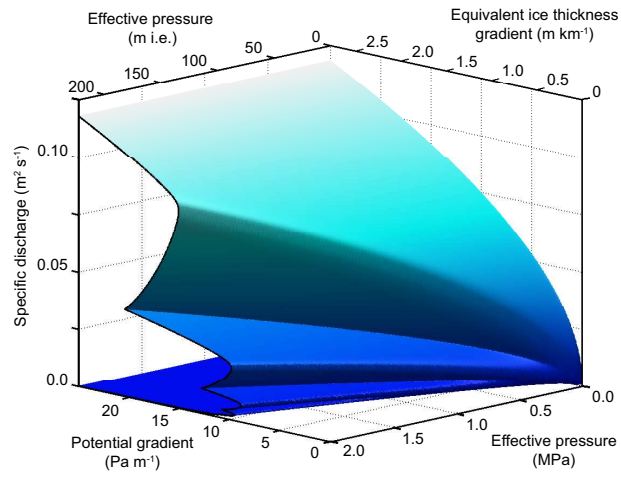


**Figure 12.** Water discharge  $Q(p_e, |\partial\phi/\partial y|)$ . As is the case for  $\bar{H}$ ,  $Q$  is generally multi-valued. Stable branches of the function are shown as more reflective parts of the surface and slope that slope upward to the left. (*i.e.*, on which discharge increases with potential gradient).